Available online at www.sciencedirect.com
ScienceDirect
Comput. Methods Appl. Mech. Engrg. 294 (2015) 313–330
Computer methods in applied mechanics and engineering
www.elsevier.com/locate/cma

An assessment of the phase field formulation for crack growth

Markus Klinsmann[a,b,*], Daniele Rosato[a], Marc Kamlah[b], Robert M. McMeeking[c,d,e]

[a] Robert Bosch GmbH, Corporate Sector Research and Advanced Engineering, 70049 Stuttgart, Germany
[b] Karlsruhe Institute of Technology, 76344 Eggenstein-Leopoldshafen, Germany
[c] Materials Department and Department of Mechanical Engineering, University of California, Santa Barbara, CA 93106, USA
[d] School of Engineering, University of Aberdeen, King's College, Aberdeen AB24 3UE, Scotland, United Kingdom
[e] INM-Leibniz Institute for New Materials, Campus D2 2, 66123 Saarbruecken, Germany

Received 23 February 2015; received in revised form 26 May 2015; accepted 15 June 2015
Available online 25 June 2015

Abstract

The phase field description for crack growth and fracture is an attractive alternative to numerical methods based on discrete representations of cracks, since the phase field methodology avoids the numerically challenging monitoring of the discontinuities introduced by the crack. In particular, for the simulation of complex crack growth topologies and application to coupled systems, e.g. with thermal or electrical fields, the phase field method has shown promise. However, an accurate prediction of the crack growth initiation is mandatory for a reliable simulation of crack trajectories both in terms of load history and the path followed through the material. In this work, we therefore investigate predictions of crack growth derived from the phase field method and compare them with established relations from fracture mechanics. To implement the phase field method for crack growth, a parallelized finite element method computer code using adaptive mesh refinement is developed and implemented. Results from it are presented. For these results, pre-existing cracks are introduced into the finite element model in two ways, including their representation as discrete discontinuities and as heterogeneities in the phase field order parameter.

Keywords: Phase field; Fracture; Energy release rate; Initial crack modeling

1. Introduction

Fracture of solids is an extensively investigated phenomenon due to its detrimental consequences for structures and machines [1]. Among the most complicated aspects of the theory of fracture is the prediction of the path to be taken by one or several cracks in a specimen or structural component. Due to the complexity of the phenomena involved, one commonly relies on computational methods to approach the problem [2]. A modeling approach that allows a comparably convenient numerical implementation is the phase field method for fracture. It is identified as a promising candidate for studying intricate crack growth problems, including effects such as crack branching, kinking or merging in arbitrary geometries and dimensions [3,4].

* Corresponding author at: Robert Bosch GmbH, Corporate Sector Research and Advanced Engineering, 70049 Stuttgart, Germany.
E-mail address: markus.klinsmann@de.bosch.com (M. Klinsmann).

http://dx.doi.org/10.1016/j.cma.2015.06.009
0045-7825/

Similar to phase field methods used for other problems is the inherent existence of one or many order parameters that take defined values depending on the state and development of the phases subject to numerical smoothing, giving a continuous transition between states. In the area of fracture, the order parameter discriminates between an intact and a cracked region of the material. In contrast to discrete crack models, the phase field does not attempt to describe the crack as a geometric feature with a physical discontinuity, but as a smoothed continuum approximation with a gradient providing a transition between the intact and fractured states, taking place within a characteristic length, l [5,6].

The crucial advantage of the phase field approach is the avoidance of complicated, sophisticated techniques necessary to describe complex crack topologies in the discrete setting. Examples of such techniques are the adaptive reconstruction of the mesh through introduction of new boundaries at freshly created crack surfaces [7] and the extended finite element method (XFEM) [8], that enriches the shape functions in cracked elements by addition of a set of discontinuous ones. Also rather common is the usage of so called cohesive elements that allow displacement jumps at element boundaries and therefore restrict the crack to penetration along the corresponding element edges [9,10].

Due to the smooth character of the phase field, complicated crack patterns, as for example shown in [11–13], are in principle achievable in the setting of a standard finite element method. The easy implementation of the method resulting from this benefit has led to its utilization already beyond purely mechanical problems, for example in thermally [14] or electrochemically [15] coupled ones.

However, applying the technique to situations that involve complexities from multiphysical effects, or examining detailed crack patterns that result, for example, from dynamic crack processes, requires validation. This is particularly the case if experiments to visualize the crack trajectory are difficult or impossible to carry out and the researcher therefore has to rely on the results of computations to gain insight into how flaws propagate. The most obvious manner in which validation of the phase field methodology can be achieved is to check whether its results are in agreement with well established results from classical fracture mechanics. The present work shall thus present an examination of a typical fracture phase field formulation to check on its conformity with standard results from fracture mechanics. To our knowledge, the closest comparison of this type can be found in [16], but we judge additional results as presented below to be insightful and valuable in regard to the validity of a phase field methodology for fracture.

We begin with a short introduction into our fracture phase field formulation in Section 2 and describe its numerical implementation in Section 3. In Sections 4.1 and 4.2 respectively we then present its solutions for both a pure bending specimen and a single edge notch test in regard to predictions of the growth of a pre-defined crack. Discussions on the results are presented in Section 5 and we end with conclusions regarding our findings.

2. Model formulation

The classical energy criterion for brittle fracture developed by Griffith and Irwin [1,17,18] states that a pre-existing crack starts to grow as soon as the elastic energy in the material that can be released during crack propagation is sufficient to overcome the fracture resistance of the material. That is, to extend a crack of length a by a distance Δa, enough stored energy must be transformable into surface energy, plastic work and other dissipative forms of work required to separate the material. From a thermodynamical point of view, crack extension thus can be treated as a process that occurs to minimize a free energy composed of the stored elastic bulk energy plus the fracture energy. The foundation of the fracture phase field method through this variational approach was established in [19] and [20]. Following this, approximate solutions to the energy variation were found by introduction of a scalar field d and a length scale parameter l, so that the original fracture energy functional could be represented in a regularized form in terms of d and its gradients [21], an idea that was originally developed for problems related to image segmentation [22]. The original energy functional can then be recovered in the sense of Γ-convergence, when l tends to zero. A comprehensive overview of these topics is given in [23].

Here, we follow the formulation of rate-independent crack propagation given in [24], with modifications taken from [11]. Alternative approaches are found, for example, in [6,16].

A standard feature of a phase field method is the definition of a so called order parameter, that indicates the state of a phase present at a certain point in time $t \in \mathbb{R}$ and space $\mathbf{x} \in \mathbb{R}^{\dim}$. In our case, the two states refer to cracked and intact material and correspond to order parameter values 1 and 0 respectively, as depicted by the blue line in Fig. 1.

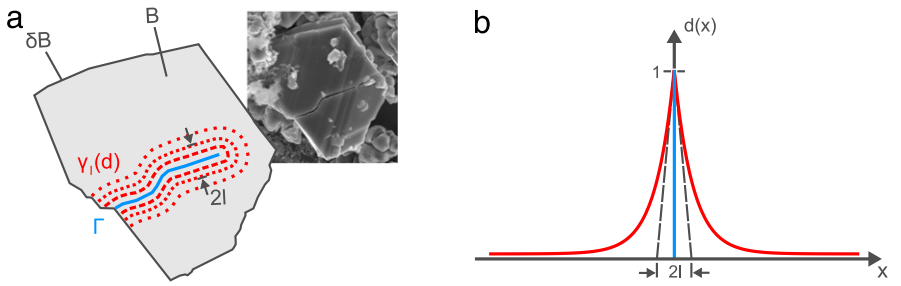

Fig. 1. (a) Schematic illustration of the encoding of a cracked region by $d = 1$ along Γ, in blue, and smoothing of the path over a length scale l, in red. The inset shows a scanning electron microscopy picture of a cracked ceramic particle. (b) One dimensional graph of the distribution of the order parameter d across a crack. (For interpretation of the references to color in this figure legend, the reader is referred to the web version of this article.)

Thus, the order parameter[1] is of the form

$$d(\mathbf{x}) = \begin{cases} 1, & \text{if material is cracked,} \\ 0, & \text{if material is intact.} \end{cases} \tag{1}$$

The second distinctive feature of the method is a spatially smoothed representation of the crack, given that x is the distance measured orthogonally from the center of the smeared crack. A typical continuous, smooth approximation of (1) in a one dimensional scenario is the exponential function

$$d(x) = e^{-|x|/l}, \tag{2}$$

with the length scale parameter $l \in \mathbb{R}^+$ determining the width of smearing of the function. As l approaches zero, a discontinuous function is recovered representing a discrete crack. The smoothing of the step-like function is depicted in Fig. 1(b). It can be shown that the function in Eq. (2) is a minimizer of the one-dimensional analog to the functional

$$W_{\text{crack}}(d) = G_c \int_{\mathcal{B}} \underbrace{\left(\frac{1}{2l} d^2 + \frac{l}{2} |\nabla d|^2 \right)}_{\gamma_l(d)} \mathrm{d}V, \tag{3}$$

subject to the condition that there is a crack at $x = 0$. Here, G_c is the Griffith-type critical energy release rate. A solution to the minimization principle

$$d(\mathbf{x}, t) = \text{Arg} \left\{ \inf_{d \in D_{\Gamma(t)}} W_{\text{crack}}(d) \right\}, \tag{4}$$

thus represents a smoothed approximation to the discrete crack at $\mathbf{x} \in \Gamma(t)$, as depicted in Fig. 1(a). The functional W_{crack} approximates the fracture energy through replacement of the integration along the crack surface $\Gamma(t)$ by a volume integration of the crack surface density $\int_{\Gamma(t)} \mathrm{d}A \approx \int_{\mathcal{B}} \gamma_l(d) \mathrm{d}V$. However, the actual position and geometry of the crack have to be determined in advance by appropriate constraints of the type

$$D_{\Gamma(t)} = \{ d \mid d(\mathbf{x}, t) = 1 \text{ at } \mathbf{x} \in \Gamma(t) \}. \tag{5}$$

In order to obtain the full evolution of the growth of the crack, the minimization principle in Eqs. (3)–(5) is replaced by one involving the total energy. Borden et al. [11] present this in the form of a total Lagrangian energy functional

$$L(\boldsymbol{\varepsilon}, \dot{\mathbf{u}}, d) = \int_{\mathcal{B}} \left(\frac{1}{2} \rho \dot{\mathbf{u}}^2 - \psi(\boldsymbol{\varepsilon}, d) \right) \mathrm{d}V - W_{\text{crack}}(d), \tag{6}$$

[1] We will use both the term order parameter and phase field to denote $d(\mathbf{x}, t)$ without any distinction.

where ρ is the density of the material, $\dot{\mathbf{u}}$ the local material velocity and $\boldsymbol{\varepsilon}$ the small strain tensor defined as the symmetric gradient of the displacements $\mathbf{u}$ by

$$\boldsymbol{\varepsilon} = \frac{1}{2}(\nabla \mathbf{u} + (\nabla \mathbf{u})^T). \tag{7}$$

The stored elastic energy density $\psi(\boldsymbol{\varepsilon}, d)$ is based on a constitutive law for an elastic linear isotropic material response. However, assuming that only tensile stress leads to crack growth, the energy density is decomposed to compressive and tensile parts via

$$\psi^{\pm}(\boldsymbol{\varepsilon}) = \frac{1}{2} L \langle \mathrm{tr}[\boldsymbol{\varepsilon}] \rangle_{\pm}^2 + G' \mathrm{tr}[\langle \boldsymbol{\varepsilon} \rangle_{\pm}^2], \tag{8}$$

where L and G' are the Lamé constants. Operating on scalars, the angle brackets are defined by $\langle x \rangle_{\pm} = \frac{1}{2}(|x| \pm x)$. Applied to symmetric tensors, they project onto the eigenspace with positive or negative eigenvalues by $\langle \boldsymbol{A} \rangle_{\pm} = \sum_i \langle \lambda_i \rangle_{\pm} \boldsymbol{v}_i \otimes \boldsymbol{v}_i$, where λ_i and $\boldsymbol{v}_i$ are the eigenvalues and corresponding eigenvectors of $\boldsymbol{A}$ respectively. The dyadic product is defined such that if $\mathbf{A} = \mathbf{v} \otimes \mathbf{w}$, then $A_{ij} = v_i w_j$. The release of elastic energy ψ at cracked locations is then modeled by multiplying the tensile part $\psi^{(+)}$ with a function, which becomes zero if the order parameter d approaches unity, so that

$$\psi(\boldsymbol{\varepsilon}, d) = [(1-d)^2 + k]\, \psi^{+}(\boldsymbol{\varepsilon}) + \psi^{-}(\boldsymbol{\varepsilon}). \tag{9}$$

Here, k is a numerical parameter chosen to stabilize the solution. Alternative approaches to distinguish between contributions to the elastic energy that come from different types of stress can be found in [25,26,6]. The Euler–Lagrange equations for the Lagrangian (6) are then used to find the evolution equation for the phase field

$$d - l^2 \nabla^2 d = 2(1-d) \frac{\mathcal{H}}{G_c / l}, \tag{10}$$

where the local history field of maximum positive elastic stored energy

$$\mathcal{H}(\mathbf{x}, t) := \max_{s \in [0,t]} \psi^{+}(\boldsymbol{\varepsilon}), \tag{11}$$

is replacing $\psi^{+}(\boldsymbol{\varepsilon})$ to ensure that the crack growth is irreversible in the sense that no crack healing can occur. The elastic energy driving the crack results from the deformation of the body when an external load is applied. As balance law, the corresponding stress distribution satisfies

$$\rho\, \ddot{\mathbf{u}}(\mathbf{x}, t) = \nabla \cdot \boldsymbol{\sigma}(\mathbf{x}, t), \tag{12}$$

which may also be derived from the Euler–Lagrange equations. The Cauchy stress is directly obtained as a partial derivative of the elastic energy density $\boldsymbol{\sigma} = \partial_{\boldsymbol{\varepsilon}} \psi$ by

$$\boldsymbol{\sigma} = g(d)\, \boldsymbol{\sigma}^{+} + \boldsymbol{\sigma}^{-}, \tag{13}$$

with the compressive and tensile parts given by

$$\boldsymbol{\sigma}^{\pm} = L \langle \mathrm{tr}[\boldsymbol{\varepsilon}] \rangle_{\pm} \mathbf{1} + G' \langle \boldsymbol{\varepsilon} \rangle_{\pm}. \tag{14}$$

The coupled pair of balance equations (10) and (12), together with the constitutive relations (13) and (14), as well as the definition of the history field (11) and the kinematic relation for the strain (7) represent a well-posed mathematical problem for the phase field d and the mechanical displacements $\mathbf{u}$. The necessary boundary conditions to this problems are given by $\mathbf{u} = \bar{\mathbf{u}}$ on ∂B_u and $\mathbf{t} = \boldsymbol{\sigma}\mathbf{n} = \bar{\mathbf{t}}$ on ∂B_t, as well $\nabla d \cdot \mathbf{n} = 0$ on ∂B, where $\partial B_u \cap \partial B_t = \emptyset$ and $\partial B_u \cup \partial B_t = \partial B$. Additionally, the initial conditions for the displacements are given by $\mathbf{u}(t_0) = \dot{\mathbf{u}}(t_0) = 0$. Approaches on how to model the initial cracks are presented in Section 4.

3. Numerical implementation

Eqs. (10) and (12) were implement in a `C++` code using the finite element library deal.II v8.1 [27,28], an open source system aimed at the development of finite element codes for efficient solution of partial differential equations using

adaptive meshes. It further supports parallel computations and provides interfaces to the software projects Trilinos [29] and PETSc [30]. These links give access to a large set of numerical solvers and preconditioners from which we chose the algebraic multigrid (AMG) preconditioner from Trilinos together with a conjugate gradient (CG) solver, which is a suitable combination for symmetric, positive definite systems and provides better parallel scalability than using direct solvers.

Due to the spectral decomposition of the strain tensor, the equations implementing conservation of linear momentum become nonlinear. To obtain optimal convergence, we implemented a backtracking line search method for finding the optimal step width [31]. The phase field and linear momentum equations are then solved in an alternating procedure for every time step until their combined residual norm falls below a specific threshold. The number of these iterations is utilized as a criterion for triggering a time adaptive scheme. As soon as the number of iterations exceeds a pre-defined value, the time step is decreased and the current step recalculated. Hence, crack initiation is never missed due to overly large time steps. During the iterations, the history field is always first restored from the last time step and then updated consistent with the current maximum tensile energy. In this way, the irreversibility condition does not apply to intermediate solutions so that updated values of $\mathcal{H}$ are always an outcome of a fully converged time step.

In addition to the time adaptivity, a mesh adaption algorithm is developed, that is based both on a physical argument, incorporating the momentary tensile elastic energy, and a numerical criterion, taking into account the product of the norm of the phase field gradient and the element size. The algorithm assures that the mesh is refined prior to the nucleation or growth of a crack and allows coarsening in intact regions that experienced high tensile stress in previous time steps.

The physical quantity driving crack growth is the local tensile elastic energy $\psi^+(\boldsymbol{\varepsilon})$, as given in Eq. (8). It enters the evolution equation of the phase field (10) through the history field $\mathcal{H}$. Hence, before crack growth is initiated, $\psi^+(\boldsymbol{\varepsilon})$ is expected to increase locally. This increase is used as a criterion to trigger mesh refinement before a crack begins to propagate. The tensile elastic energy $\psi^+(\boldsymbol{\varepsilon})$ is therefore compared with a threshold value ψ_{thresh}, so that an element is refined if $\psi^+(\boldsymbol{\varepsilon}) > \psi_{\text{thresh}}$. In an initially coarse mesh, small regions of large tensile elastic energy may not be captured sufficiently. On the other hand, it is computationally desirable to generate a very fine mesh only in regions of maximum tensile elastic energy, i.e. in regions where a crack is expected to grow. To manage both requirements, the threshold is taken as a function $\psi_{\text{thresh}} = \psi_{\text{thresh}}(n)$, that depends on the number of refinements n of the element in question. It is small for low number of refinements and increases with n. Replacing the number of refinements n by the element size h, it reads

$$\psi_{\text{thresh}}(h) = \left(\psi_{\text{up}} - \psi_{\text{low}}\right)\left(1 + \frac{\ln(h_{\min})}{\ln(h_{\text{ratio}})} - \frac{\ln(h)}{\ln(h_{\text{ratio}})}\right)^r + \psi_{\text{low}}. \tag{15}$$

Here, ψ_{up} is the upper threshold for which elements larger than $h > h_{\min}$ are further refined. Likewise, ψ_{low} is the lower boundary at which elements with $h > h_{\max}$ are refined and $h_{\text{ratio}} = h_{\max}/h_{\min}$ is the ratio of the threshold element sizes. The exponent r can be adjusted to determine the spatial extent of the refinement region, e.g. to obtain large areas with only weak refinement or a small zone with highly refined elements. If the tensile energy is lower than $\psi_{\text{thresh}}(h/2^{\Delta n})$, with $\Delta n > 1$ defining a passive region between refinement and coarsening, the element is coarsened.

The threshold function provides an energy based criterion for mesh refinement or coarsening. However, in situations, where a crack has developed and consequently the tensile energy is decreasing, the threshold function is not sufficient to guarantee that the mesh remains fine enough. For this reason, a second measure is introduced that assures that gradients of the phase field are always sufficiently accurately resolved. The maximum gradient in the one dimensional solution in Eq. (2) is $d'_{\max} = \max_{\mathbf{x}\in\mathcal{R}} |d'| = 1/l$. If $h = k\,l$, this means that the product of phase field gradient and element size $d'_{\max} h = k$ is constant. We generalize this observation to two and three dimensions and impose the second criterion, which triggers refinement if the product of the norm of the gradient of the phase field, i.e. $|\nabla d|$ and the element size h is larger than a defined constant $|\nabla d|\, h > k_1$. Typically, k_1 is set slightly below one half of l. In the same way, coarsening is allowed if $|\nabla d|\, h < k_2$, where $k_2 > l$.

The combination of both conditions generates a mesh that is sufficiently fine to not influence the solution of the problem, and saves computation time by coarsening of regions that do not require a fine resolution. The full adaptive scheme resulting from these conditions is described in Appendix A.2.

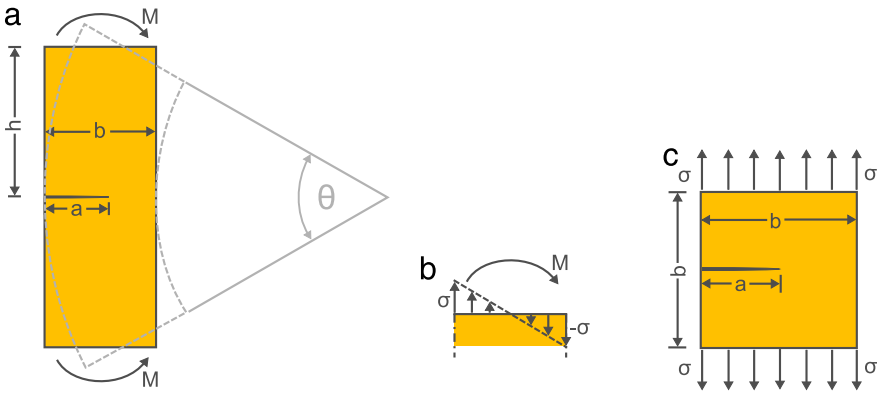

Fig. 2. (a) Pure bending specimen with initial crack length a, height $2h$, width b and bending angle θ. (b) Illustration of relation between bending moment M and normal stress σ along upper and lower boundary of the bending specimen. (c) Single edge notch specimen with side length b and applied normal stress σ.

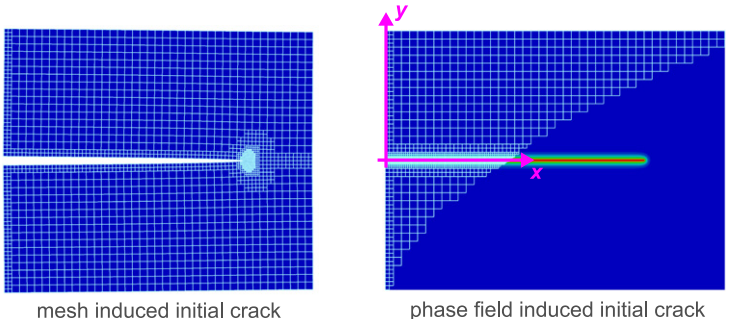

Fig. 3. Different approaches for introducing the initial crack. Both figures are depicted before the crack begins to grow. (Left) *Mesh defined initial crack*, modeled with free boundaries of the mesh. (Right) *Phase field induced initial crack*, introduced through initial history field $\mathcal{H}_0$.

4. Results

Two different setups are chosen to investigate the effectiveness of this particular fracture phase field implementation in solving typical fracture mechanics problems. The first is a pure bending specimen and the second is a load controlled uniaxial stretch specimen, as depicted in Fig. 2(a) and (c) respectively. Both specimens are studied in two dimensions under plane strain. Further descriptions and analytic fits to numerical solutions for these problems can be found in [32].

In both specimens an initial edge crack with length a is introduced. Two different approaches are examined for this step. In one approach, the crack is modeled with free boundaries starting at the edge and reaching into the interior of the mesh, as, for example, utilized in [24]. We will denote this approach as *mesh induced initial crack*. An example of it is shown on the left hand side of Fig. 3.

Alternatively, we prescribe the crack through the phase field by defining an initially non-zero history field of the form

$$\mathcal{H}_0 = \alpha\, e^{-(y/\beta)^2} \times \begin{cases} 1, & x < a \\ e^{-(x/\beta)^2}, & x \geq a, \end{cases} \tag{16}$$

for a crack that is located at $y = 0$ and extends from the edge at $x = 0$ to $x = a$. The phase field is then allowed to relax in a number of iterations to the given history field, combined with an adaptive re-meshing of the initially uniform mesh. The idea behind this approach is to develop a phase field that resembles the form that it commonly takes on when it describes a crack that has grown due an external load. In those situations, the history field $\mathcal{H}$ at the crack is typically a very localized field with large values at the peak location of the phase field and a steep decrease away from it. The amplitude in Eq. (16) is therefore set to $\alpha = 10^4$ and the width $\beta = l/10$.

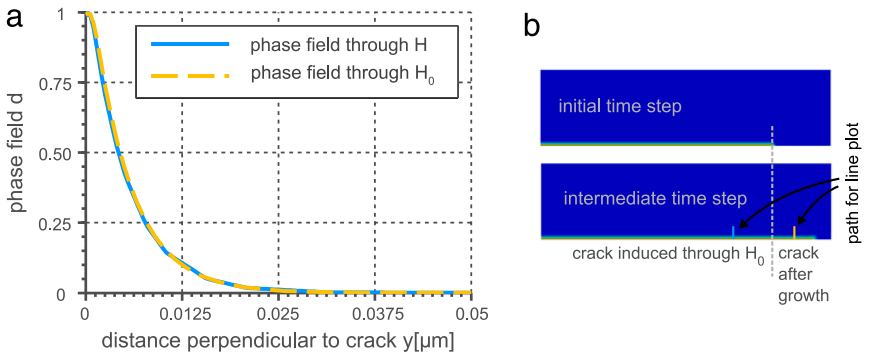

Fig. 4. (a) Decay of the order parameter d along a line perpendicular to the crack path taken at two locations along the crack, as marked in (b). At the first location, the phase field is initially induced through H_0. The second location is somewhere between the initial and final crack tip position, i.e. where the phase field is driven through elastic energy growing the crack.

In contrast to the approach in [16], directly setting the initial phase field $d_0(\mathbf{x})$ is not applicable in our formulation. This results from the fact, that the irreversibility condition only enters the history field $\mathcal{H}$. An initially zero history field would therefore always lead to a vanishing order parameter d, independent of its initial condition. The method is also more versatile than using nodal constraints of Dirichlet type for the order parameter since in this case the location of the crack would have to coincide with nodes of the mesh. Further, it can be generalized to model more complex initial crack geometries but a discussion of the details is beyond the scope of this paper.

We believe our approach to be a reasonable since the form of the resulting phase field in regions that are induced by $\mathcal{H}_0$ is identical to that obtained when the phase field has grown because of tensile stress. This can be seen in Fig. 4 where we plot the value of the order parameter d at a location, where a crack is initially induced through $\mathcal{H}_0$ and at a location through which the crack grows thereafter. The difference is negligible. In addition, the influence of the parameters α and β on the actual shape of the phase field proves to be negligible as long as the amplitude α of $\mathcal{H}_0$ is high enough and its decay, controlled by beta, is faster than the one from the phase field for a grown crack. An alternative realization of the history variable induced pre-crack can be found in [11]. This approach will be called the case of a *phase field induced initial crack*. It is depicted on the right hand side of Fig. 3.

The specimens are slowly bent or stretched, with the angle or load being proportional to time. The main focus then lies in finding the characteristic critical quantities, such as applied stress or imposed angle, that lead to growth of the crack, and comparing them with analytic results from the literature for quasistatic behavior. The quasistatic growth condition for a crack under mode I loading is such that the relevant stress intensity factor

$$K_I = \sigma \sqrt{\pi a}\, F(a/b) \tag{17}$$

must be equal to the plane strain fracture toughness K_{Ic}. The characteristic stress measure σ and shape factor $F(a/b)$ are specific to the respective specimen and will be given later. In terms of energy release rates, this means that if

$$G = \frac{K_I^2}{E'} \tag{18}$$

reaches the toughness G_c, the crack starts to extend. For plane strain conditions, the parameter E' is defined as $E' = E/(1-\nu^2)$. The quantities are thus compared with the relations (17) and (18), calibrated to the specific specimens investigated.

In most situations investigated, crack growth takes place in an unstable fashion. This means that as soon as the phase field starts to evolve and the crack extends, the local tensile strain energy at the crack tip does not decrease fast enough to arrest crack growth and a new equilibrium cannot be found. Hence, although the applied boundary conditions remain fixed, the crack continues to propagate. Its extension per time step is therefore only controlled by inertia. As a result, the number of alternating iterations between the elastic and phase field computations, as described in Section 3, exceeds a defined threshold. Due to the time adaption algorithm, the time step consequently decreases drastically by orders of magnitude. After a number of time adaption steps, the extension of the crack per time step becomes small enough, so that the prescribed maximum number of iterations for the elastic and phase field

computations is sufficient to find the current dynamic equilibrium, and the time step stabilizes again. We take this rapid drop in the time step to be an objective criterion for determining the instant of crack growth initiation and for selecting the respective critical quantities. Since this drop does not occur during stable crack growth, we also exploit it for differentiating between the onset of stable and unstable crack extension.

For crack growth initiation, the length of the crack is defined by the method of introducing it. For the *mesh induced initial crack*, it is given through the length of the free surface; for the *phase field induced initial crack*, it is prescribed by a in the definition of the initial history field, given in Eq. (16). To measure the crack length during crack growth, as in the stable growth regime for the bending test, a different definition of the crack length has to be found. The crack is therefore taken to terminate with its tip at the location where $d = 0.95$. The crack length is measured accordingly and the corresponding critical values of parameters are extracted from the output with this given definition of crack length. We concede that the chosen value of the order parameter to define the crack tip is somewhat arbitrary. Borden et al. [11], for example, use a value of $d = 0.75$ in their work to find the crack tip when identifying its velocity. Furthermore it is not fully consistent with the definition of the crack length for crack growth initiation. However, we emphasize that the ambiguity in defining the crack tip is an intrinsic property of the phase field formulation for fracture and discuss its consequences in Section 5.

4.1. Pure bending specimen

The pure bending specimen is selected as a test case since it allows the study of both stable and unstable crack growth. The characteristic stress of Eq. (17) is defined through the bending moment, see Fig. 2(b), by

$$\sigma = \frac{6M}{b^2} \tag{19}$$

and the shape factor is taken from [32] as

$$F(a/b) = \sqrt{\frac{2b}{\pi a}\tan\frac{\pi a}{2b}}\,\frac{0.923 + 0.199(1-\sin\frac{\pi a}{2b})^4}{\cos\frac{\pi a}{2b}}, \tag{20}$$

giving better than 0.5% accuracy in K_I in terms of Eq. (17) for any a/b. Inserting this function into (17) yields a right hand side, which is monotonically increasing with crack length. This means that for a given critical stress intensity factor, the stress necessary to generate crack growth is monotonically decreasing with the crack length. A moment or force controlled bending test thus always leads to a situation of unstable crack growth. In contrast, if the bending is prescribed through the angle, both a stable and an unstable regime can be found.

The total bending angle can be separated into two parts, a bending that assumes a perfect rectangular specimen without a crack and a contribution due to the crack

$$\theta = \theta_{\text{uncracked}} + \theta_{\text{crack}}. \tag{21}$$

We prescribe the angle on the upper boundary for which $h/b = 3$. Since the aspect ratio $h/b = 3$ enables use of beam theory, the first part can be deduced to be

$$\theta_{\text{uncracked}} = \frac{\sigma}{E}(1-\nu^2)\frac{4h}{b}. \tag{22}$$

For the crack contribution we use the solution from [32], which comes with an accuracy of better than 1% for any a/b. It reads

$$\theta_{\text{crack}} = \frac{\sigma}{E}(1-\nu^2)\,4S(a/b), \tag{23}$$

with

$$S(a/b) = \left(\frac{a/b}{1-a/b}\right)^2 \sum_{i=0}^{4} q_i (a/b)^i \tag{24}$$

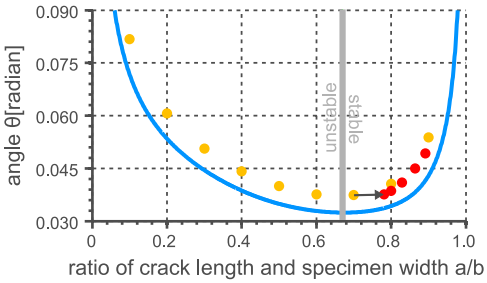

Fig. 5. The solid blue line shows the equilibrium angle at which $G = G_c$ depending on the ratio of crack length a to specimen width a/b, as obtained from Eq. (25). Yellow dots mark points of crack initiation obtained from phase field simulations with a *mesh induced initial crack*. The red dots were extracted during stable crack growth from an initially unstable simulation (yellow dot with arrow). The gray line describes the theoretical boundary between stable and unstable growth. (For interpretation of the references to color in this figure legend, the reader is referred to the web version of this article.)

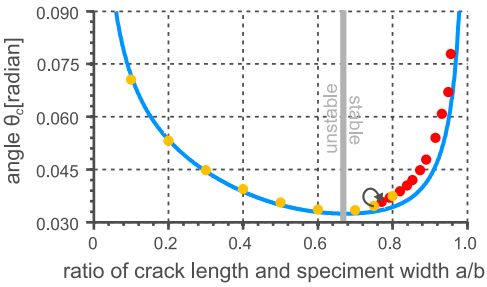

Fig. 6. The solid blue line shows the equilibrium angle at which $G = G_c$ depending on the ratio of crack length a to specimen width a/b, as obtained from Eq. (25). Yellow dots mark points of crack initiation obtained from simulations with a *phase field induced initial crack*. The red dots were extracted during stable crack growth from an initially stable simulation (yellow dot with arrow). The gray line describes the theoretical boundary between stable and unstable growth. (For interpretation of the references to color in this figure legend, the reader is referred to the web version of this article.)

and $q_0 = 5.93$, $q_1 = -19.69$, $q_2 = 37.14$, $q_3 = -35.84$ and $q_4 = 13.12$. Combining Eqs. (21)–(24) and replacing the stress by (17) and (18), we obtain

$$\theta_c = \frac{4}{\pi a}\frac{1}{F(a/b)}\left(\frac{h}{b} + S(a/b)\right)\sqrt{\frac{G_c}{E}(1-\nu^2)} \tag{25}$$

as the equilibrium angle at which the energy release rate is equal to the critical one given a crack length a. The dimensions of our specimen are set to $b = 1$ µm and $h = 3$ µm, Young's modulus is $E = 93$ GPa, the Poisson ratio $\nu = 0.3$ and the material density $\rho = 4140$ kg/m^3. The critical energy release rate is defined by $G_c = 1.2$ J/m^2. The corresponding curve is plotted in both Figs. and 6. The angle is prescribed through a multi-point constraint. For the upper boundary, the vertical displacement of the center node u_y^0 located at $x = 0$ and $y = h$ is unconstrained and vertical displacements of all other nodes are fixed by $u_y(x) = u_y^0 - \frac{\theta}{2}x$. The edge is therefore free to move vertically while keeping the prescribed angle, so that no net axial force acts on it. The boundary condition on the lower edge is applied correspondingly. The rate of the bending angle was set to $\dot{\theta} = 10^{-4}$ rad/s. The loading history can therefore be considered to be quasi-static.

We observe that under rotation controlled boundary conditions, a regime of stable crack growth exists for $a/b \geq 0.67$. In this region, a crack that has grown by a distance Δa, only further extends if the rotation is increased. In contrast, for smaller ratios of a/b, a crack that has once started to grow, does not stop until it reaches the corresponding angle in the stable region at which the energy release rate is again $G = G_c$. This process is depicted in Fig. 7. From our experience, unstable crack propagation can only be predicted accurately by a dynamic analysis. Otherwise, an erroneous evolution of the phase field may occur, e.g. by a significantly larger smoothing of d than expected from the length scale parameter. This broadening effect has also been mentioned in [24].

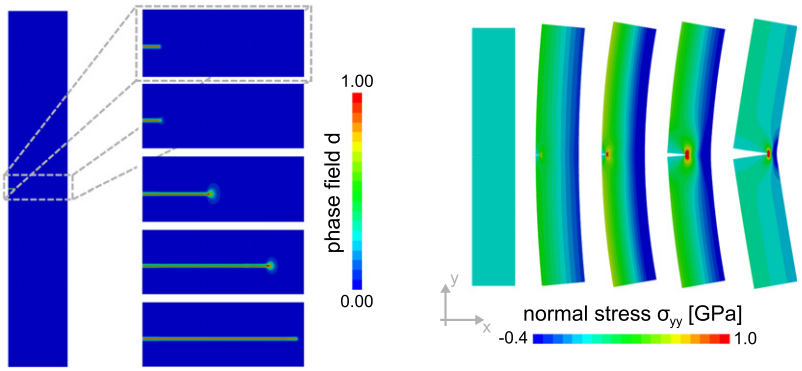

Fig. 7. Illustration of results for the bending specimen. (Right) Normal stress in y-direction is plotted for a number of bending angles. The displacements are scaled by a factor of 5 to show the deformation of the specimen exaggerated. (Left) During bending an initially small crack propagates in an unstable fashion and stops at a location close to the opposite free edge. An order parameter of $d = 1$ marks cracked regions, whereas $d = 0$ corresponds to intact regions.

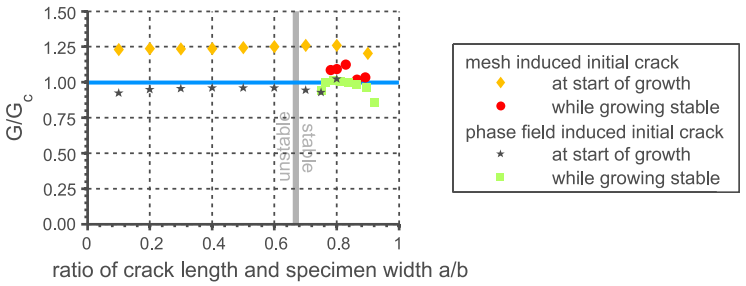

Fig. 8. Computed energy release rate G normalized by the critical energy release rate G_c. Data points correspond to those shown in Fig. 5 and Fig. 6. Again, the gray line describes the theoretical boundary between stable and unstable growth. *Mesh induced initial crack*: The start of crack growth (yellow diamonds) is always unstable. The red dots indicate the values of G for cases where the growth of a *mesh induced crack* has changed to a stable regime. *Phase field induced initial crack*: The start of crack growth (black stars) is unstable or stable in agreement with the theoretical boundary. The values of G computed during stable crack growth are denoted by the green squares. (For interpretation of the references to color in this figure legend, the reader is referred to the web version of this article.)

As a second quantity to evaluate the predictions on crack growth obtained from the phase field simulations, we compute the energy release rate G for the data points presented in Figs. 5 and 6. We combine Eqs. (17) and (18) yielding

$$G = \sigma^2 \pi a \, F^2(a/b) \tag{26}$$

and insert the measured crack length and applied stress σ, as given by Eq. (19). The results are normalized by the input parameter G_c and plotted in Fig. 8.

4.2. Single edge notch specimen

To strengthen the findings on the predictions of the phase field method for crack growth obtained from the observations on the pure bending specimen, a second series of simulations is run for a single edge notch specimen with force controlled boundary conditions. The corresponding geometry, shown in Fig. 2(c), represents the most simple setup to study crack growth. Due to its unstable behavior at crack initiation, it allows determination of the critical stress very precisely and is therefore suitable for examining the influence of the length scale parameter l on the numerical results. Other works, investigating this kind of specimen, can be found in, for example, [16,24].

The characteristic stress of Eq. (17) is equal to the normal stress in the y-direction $\sigma = \sigma_{yy}$ at the upper boundary and the geometry function is again taken from [32]

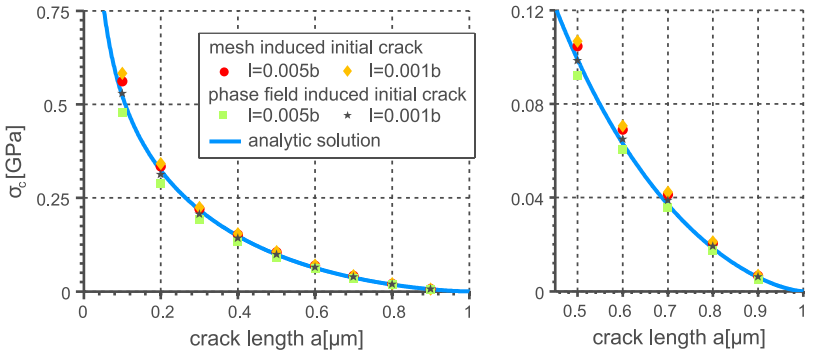

Fig. 9. Applied external stress for varying crack length a at instance when $G = G_c$. Colored markers are stress values taken from simulations at the moment when the crack starts to grow. The diagram on the right is a magnification of the points with larger initial crack length. (For interpretation of the references to color in this figure legend, the reader is referred to the web version of this article.)

$$F(a/b) = \sqrt{\frac{2b}{\pi a}\tan\frac{\pi a}{2b}}\,\frac{0.752 + 2.02(a/b) + 0.37\left(1-\sin\frac{\pi a}{2b}\right)^3}{\cos\frac{\pi a}{2b}}, \tag{27}$$

with better than 0.5% accuracy in $F(a/b)$ for any a/b. The width of the specimen is $b = 1$ μm, Young's modulus is set to $E = 93$ GPa, Poisson ratio to $\nu = 0.3$, the material density to $\rho = 4140$ kg/m^3 and the critical energy release rate to $G_c = 1.2$ J/m^2.

The load on the specimen is increased slowly with time until the crack starts to grow. We again take the drop in the time step resulting from the time adaption scheme to determine the moment of crack growth initiation in the phase field simulation. The corresponding critical stress is presented in Fig. 9 for both *mesh* and *phase field induced initial cracks*, for different initial crack lengths a and two values of the length scale parameters l. The results are compared with the theoretical stress at which $G = G_c$. For the latter, Eqs. (17) and (18) are combined to give

$$\sigma_c = \sqrt{\frac{G_c E}{1-\nu^2}}\,\frac{1}{\sqrt{\pi a}}\,\frac{1}{F(a/b)}. \tag{28}$$

We impose the critical stress as boundary condition in a second, purely elastic simulation without phase field to determine the energy release rate using the J-integral method. For the evaluation of J, we use the commercial tool COMSOL Multiphysics®. For the presented setting J is a path-independent line integral. Given a counterclockwise path S around the tip of a crack, it reads

$$J = \int_S \left(w\,\mathrm{d}y - t_i \frac{\partial u_i}{\partial x}\mathrm{d}s \right), \tag{29}$$

with the length increment $\mathrm{d}s$ along the contour Γ, the strain energy density $w = \int_0^{\varepsilon_{ij}} \sigma_{ij}\mathrm{d}\epsilon'_{ij}$ and the traction vector $t_i = \sigma_{ij} n_j$ in normal direction $\mathbf{n} = n_i \mathbf{e}_i$ to the path [1]. For the given setting of a linear elastic material under quasi-static conditions, the magnitude of the J-integral is equal to the energy release rate, $J = G$. The so computed energy release rates are plotted in Fig. 10.

In order to explore the influence of the length scale parameter l on the predictions of the phase field method more closely, simulations with l ranging from $0.005\,b$ to $0.0005\,b$ are run for an initial crack length of $a = b/2$, including both methods of introducing the initial crack. The resulting energy release rates are shown in Fig. 11.

5. Discussion

5.1. Pure bending specimen

Comparing the critical angle extracted from simulations with the analytic solution in Fig. 5 in the unstable regime, we observe a non-negligible discrepancy between 13.3% and 14.6% for computations with a *mesh induced initial crack*. As will be shown for the single edge notch specimen, this discrepancy does not result from the mesh or the

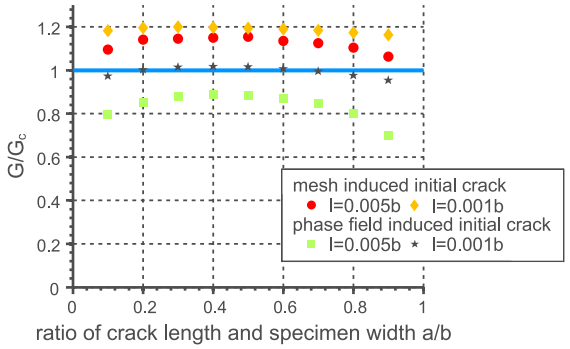

Fig. 10. Normalized energy release rates G/G_c at crack growth initiation computed via the J-integral method against initial crack length a for two values of the length scale parameter l and both methods of introducing the initial crack.

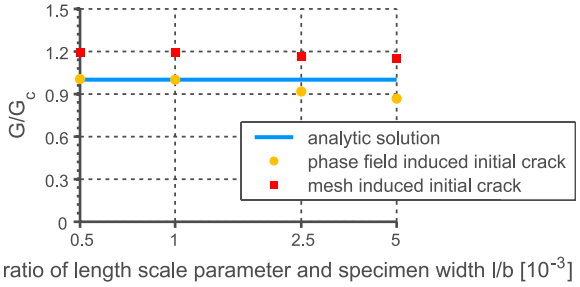

Fig. 11. Normalized energy release rates G/G_c computed via J-integral method against length scale parameter l for both methods of introducing the initial crack.

staggered numerical implementation. We attribute it to an initial build-up phase required to create a region of $d = 1$ at the crack tip, that significantly postpones the crack initiation in the sense of an evolving phase field.

In contrast, the numerical results for the *phase field induced initial crack* are in very good agreement with the analytic ones for the case of unstable crack growth, see Fig. 6. The error in θ_c is always below 2.1% in the unstable regime.

In the stable regime, the results from the two methods of introducing the crack are closer to each other, when the data is extracted during crack growth. This agrees with our expectations, since in both cases the growth of the crack is described through the same extension of the non-zero phase field region. However, there is a slight offset between numerical and analytical data, even for the *phase field induced initial crack*. One reason for this difference might lie in the non-unique way that the length of a phase field crack may be measured during crack growth, resulting from the continuous increase of the order parameter at the crack tip from zero to unity. To make this point clearer, some numbers shall be given here. For all bending specimen calculations, the crack tip was defined to be located at $d = 0.95$. However, if we measure the crack tip instead at $d = 0.5$ ($d = 0.1$), the crack length would be longer by $\Delta a \approx 0.005\, b$ ($\Delta a \approx 0.018\, b$). To estimate, how large the effect of the criterion on the error in terms of the bending rotations is, we compute the Taylor expansion of Eq. (25) to first order in a yielding

$$\Delta\theta_c = \left| \frac{4}{\pi a} \frac{1}{F(a/b)} \left[-\left(\frac{1}{a} + \frac{1}{b} \frac{F'(a/b)}{F(a/b)} \right) \left(\frac{h}{b} + S(a/b) \right) + \frac{1}{b} S'(a/b) \right] \right| \times \sqrt{\frac{G_c}{E}(1-\nu^2)}\, \Delta a. \tag{30}$$

For a crack length of $a = 0.914\, b$ and an error of the crack length of $\Delta a \approx 0.005\, b$ ($\Delta a \approx 0.018\, b$), taken from a simulation with a phase field induced pre-crack, this gives a relative error in the angle of around $\Delta\theta_c/\theta_c \approx 5.4\%$ ($\Delta\theta_c/\theta_c \approx 19.5\%$). The actual relative error from a phase field computation with a crack of this length is $|\theta_c^{\text{num}} - \theta_c^{\text{ana}}|/\theta_c^{\text{ana}} \approx 18\%$. The uncertainty in measuring a is therefore believed to contribute a significant fraction of the discrepancy between the results from the phase field calculation and that from the fracture mechanics analysis

of the problem based on Eqs. (17), (19) and (20). This issue is also further discussed in Section 5.2 for the stretch specimen. In the unstable regime, we observe good agreement for the *phase field induced crack*. The energy release rate is only slightly underestimated, by less than 10%. In contrast, for the *mesh induced initial crack*, G deviates from G_c by around 25%. In the stable region, both methods of introducing the crack give results that lie very close to each other.

A second contribution to the discrepancy may come from finite values of the order parameter in regions far away from the crack. It is notable that the order parameter is perceptibly above zero in the ligament ahead of the crack tip. For example, in the example mentioned above with $a = 0.914\,b$, the order parameter is $d = 0.01$, if extracted at the compressive fiber on the right hand side of the specimen in the extension of the crack. Treating d as a damage parameter in the sense that we can define an effective elastic modulus given by $E^* = (1-d)^2 E$ [33], this would mean a decrease of around 2% for the stiffness of the material. Given that this location is more compliant, the applied moment required to bend the specimen by a certain angle is decreased. This means, that the actual stress acting at the crack tip, is lower than expected for a given bending angle. For the simulations with a *mesh induced initial crack*, the value of d is larger by around 5% at the free surface beyond the ligament leading to a decrease in stiffness of the same order. It is difficult to estimate if this small difference can explain the slightly larger offset for the *mesh induced initial crack*. An additional influence could come from the initially unstable crack growth even in the stable regime, as described below. The growth velocity affects the shape of the phase field, as for example mentioned in [11], and could therefore also have an impact on the results.

Interestingly, although the critical bending angle is generally overestimated for these points, the energy release rate is quite accurate. We ascribe this to a compensating effect due to the underestimation of the bending moment, as described above. The non-zero values of d at presumably intact regions, leading to this underestimation, are strongly dependent on the history of the calculation due to the irreversibility condition in $\mathcal{H}$. For the *mesh induced initial crack*, where crack initiation generally starts later than it should, regions away from the crack may experience higher stress than for the *phase field induced initial crack*. Hence, in this case, the order parameter should be slightly larger in intact regions. To verify this hypothesis, we pick one simulation for each method of describing the initial crack, find the times where the crack has grown to the same extent and study the magnitude of d in regions away from the crack. We find, that for the *mesh induced initial crack* the order parameter is larger by around 3–5% in intact regions. This may lead to the larger offset of the data points associated with stable growth in Fig. 5 compared to Fig. 6. The argument might also explain the discrepancy in computing G, if we assume that the overestimation of the crack length a, as defined through the order parameter d, has a more dominant effect than the underestimation of σ.

Two mechanisms leading to deviations of the numerical results are identified, that apply to the situation of a *phase field induced initial crack* or when the crack is already growing from a *mesh induced initial crack*. A global one stemming from a non-zero phase field at locations that should actually be perfectly intact and a local one from the inaccuracy of measuring the crack length. Both issues, in particular the latter one, can be eased by choosing a smaller length scale parameter l. As described above, for the value of $l = 0.005\,b$ that we used, the outcome of the simulations is in good agreement with solutions from classical fracture mechanics.

In contrast, crack initiation for a *mesh induced initial crack* occurs always with a significant delay. Both the energy release rate and the critical bending angle are therefore overestimated. An overestimation of the critical failure load was also reported by Bourdin [34], who presents a backtracking algorithm in order to overcome this deficiency. We believe this to be a result of an initial build-up phase, which the phase field has to undergo before true crack growth can initiate. As a matter of course, this build-up is not required if the initial crack is already described through the phase field. A critical consequence of the initial overestimation of G_c is a predicted crack growth that is always initially unstable. This can also be observed in Fig. 5. The yellow data point at the tail of the arrow, used as the starting point for the stable results depicted by red, gives an initial spurt of crack growth that directly jumps to the first stable result (in red) without significant change of the bending angle (horizontal arrow). This behavior is not found with the *phase field induced initial crack. In this case, the simulation predicts entirely stable crack growth when the initial crack length is in the stable regime. For this reason, the yellow and red data points in Fig. 6 lie on the same curve.* This finding undermines the claimed capability of the fracture phase field method to find and accurately describe crack initiation at arbitrary locations in a specimen.

5.2. Single edge notch specimen

The most accurate results in terms of the predicted critical stress, shown in Fig. 9, are obtained in this case with the *phase field induced crack* and $l = 0.001\,b$. The relative error $\Delta\sigma_c = (\sigma_c^{\text{phase field}} - \sigma_c^{\text{analytic}})/\sigma_c^{\text{analytic}}$ of the critical stress $\sigma_c^{\text{phase field}}$ resulting from the phase field simulations with respect to the calculated one, $\sigma_c^{\text{analytic}}$, from Eq. (28) ranges between 0.4% and 5.2%. Computations with $l = 0.005\,b$ generate predictions with a similar accuracy for both the *phase field* and *mesh induced crack* of up to 11.8% and 11.3% respectively. However, the least accurate results of $\Delta\sigma_c \approx 14.5\%$ are obtained from the *mesh induced crack* with the smaller value of the length scale parameter $l = 0.001\,b$. This behavior is unexpected since it does not allow the improvement of predictions from phase field simulations by choice of numerical parameters that result in a better shape of the phase field more closely resembling the discrete nature of a crack. This is further discussed in terms of energy release rates G below.

As can be seen in Fig. 11, the predictions of the phase field simulations with respect to the obtained value of G are quite satisfactory for the case of a *phase field induced crack* and a small length scale parameter l. This was already reported in [16], see in particular FIG. 6 of their work. For example, the computed energy release rate G for $l = 0.001\,b$ is only 1.6% below the critical one G_c. For the corresponding simulations with different initial crack lengths a, the relative error $\Delta G = (G - G_c)/G_c$ ranges between 0.2% and 4.5%. The energy release rate is slightly underestimated for very small and large cracks, as shown in Fig. 10.

The tendency is the same for $l = 0.005\,b$, but the results become less satisfactory. The energy release rate G lies around 11% to 30% below G_c. This underestimation is again attributed to the overestimation of the crack length due to the diffusive representation of the crack in the phase field method. For example, in the simulations with $l = 0.005\,b$, the phase field drops to $d = 0.5$ ($d = 0.1$) at a distance of $\Delta x = 0.011\,b$ ($\Delta x = 0.027\,b$) from the crack tip when crack growth is just about to start. By varying the crack length in J-integral computations, we find that a difference in the crack length of $\Delta a \approx 0.02\,b$ can lead to an approximate change in G of 17%. This is in the range of the relative error ΔG.

The effect is less pronounced for cracks close to half the width of the specimen. For small cracks, the slope of the critical stress σ_c against the crack length becomes larger (see Fig. 9) so that small differences in the crack length have a stronger impact on the resulting σ_c. In the case of large cracks, the relative inaccuracy of the width $\Delta(b - a)$ of the ligament connecting the upper and lower part is increasing, which makes the computation of the critical stress less precise.

The simulations with a *mesh induced initial crack* show a similar, though slightly attenuated behavior. However, as before, there is a noticeable offset of 16% to around 20% between the computed energy release rates and the critical one for $l = 0.001\,b$. Moreover, the discrepancy is even intensified for smaller values of the length scale parameter l, as observable in Fig. 11, so that convergence towards the actual value of G_c is not observed. As for the pure bending specimen, we attribute the overestimation of G_c to an initial build-up of a non-zero phase field region. This presents an intrinsic drawback of the formulation since it postpones the actual crack initiation. To exclude any influence of the mesh, e.g. by not sufficiently resolving the singular stress field at the crack tip, we repeatedly reduce the element size around it. Even for an element size of $h \approx 6 * 10^{-6}\,b$ around the crack tip an improvement in terms of an earlier crack growth initiation is not recognizable.

To ensure that the error is not an outcome of the staggered implementation scheme, we extract data from a similar simulation with a monolithic solution scheme, found in Fig. 12 of [3]. In contrast to our own simulations, the results of the corresponding work are generated with displacement controlled boundary conditions. We insert the critical displacements u_c taken from the diagrams as boundary conditions and compute the energy release rate via the J-integral. The results overestimate G_c by a factor of 19% to 24%, depending on the critical displacements (input parameter is $G_c = 2.7 * 10^3$ J/m^2, extracted energy release rates are $3.22 * 10^3$ J/m^2 and $3.35 * 10^3$ J/m^2). This is even slightly higher than our results.

6. Conclusion

In this work, a study on the accuracy of predictions from a fracture phase field formulation on crack growth initiation is undertaken and compared with relations from fracture mechanics. We investigate the influence of the numerical length scale parameter l, determining the width of smoothing of the represented crack, and two methods of introducing an initial crack. Two setups are examined, a pure bending specimen and a single edge notch specimen.

Due to requirement of a fine mesh for small values of l, the model is implemented in a parallelized finite element computer code supporting both mesh and time adaption.

We find that results of the phase field simulations are in very good agreement if l is small and the initial crack is induced as a heterogeneity in the phase field through an initially non-zero history field (*phase field induced initial crack*). Predictions become less satisfying for large values of l. In situations, where the initial crack is prescribed through free surfaces of the mesh (*mesh induced initial crack*), predictions from the phase field simulations deviate significantly from analytic relations found in the literature. This is neither a consequence of an overly coarse mesh, nor of the staggered implementation scheme, and can also not be resolved using a smaller value of l.

Due to the advantages of the phase field approach for simulating complex crack topologies and in coupled applications with multiphysical phenomena, the method is worth considering as an alternative or in addition to established discrete fracture techniques. Accurate results should be obtained if initial cracks are introduced in the manner described above, i.e. with a phase field induced initial crack with a small value of l. However, small values of the length scale parameters l pose computational demands that must not be underestimated and the step of reducing the numerical effort by choosing larger values of l must be taken with care. Considering the results from the *mesh induced crack*, the capability of the presented fracture phase field formulation to find and accurately describe crack initiation at arbitrary locations in a specimen is disproved. To overcome this difficulty, further development of the method is required.

Acknowledgments

The presented results were mainly achieved during a visit of four months in the group of Prof. Robert McMeeking at the University of California, Santa Barbara. This stay was financially supported by a scholarship of the Karlsruhe House of Young Scientists (KHYS).

Appendix

A.1. Finite element implementation

In order to obtain numerical solutions of the system of partial differential equations by means of a finite element method, Eq. (12) was time integrated using an implicit Backward-Euler method and then, along with Eq. (10), cast into the form

$$G_d(d,\mathbf{u}) = \int_{\mathcal{B}} \mathrm{d}V \left(\frac{G_c}{l} + 2\mathcal{H}\right) d\,\delta d + \int_{\mathcal{B}} \mathrm{d}V\, G_c l\, \nabla d \cdot \nabla(\delta d) - 2\int_{\mathcal{B}} \mathrm{d}V \mathcal{H}\,\delta d = 0, \tag{A.1}$$

$$G_{\mathbf{u}}(\mathbf{u},d) = \int_{\mathcal{B}} \mathrm{d}V \frac{\rho\,(\mathbf{u}-\mathbf{u}_n)}{\Delta t_{n+1}^2}\delta\mathbf{u} - \int_{\mathcal{B}} \mathrm{d}V \frac{\rho\,(\mathbf{u}_n-\mathbf{u}_{n-1})}{\Delta t_{n+1}\Delta t_n}\delta\mathbf{u} + \int_{\mathcal{B}} \mathrm{d}V \boldsymbol{\sigma} : \delta\boldsymbol{\varepsilon} - \int_{\partial\mathcal{B}} \mathrm{d}S\, \bar{\mathbf{t}}\cdot\delta\mathbf{u} = 0. \tag{A.2}$$

Here δd and $\delta\mathbf{u}$ are variational test functions as used in the Galerkin method, $\mathbf{u}_n$ and $\mathbf{u}_{n-1}$ denote the displacement field of the last and second last time step t_n and t_{n-1} respectively, and Δt_{n+1} and Δt_n are the corresponding time step sizes. Quantities without index are taken at the current time t_{n+1}. The coupling between the weak forms for the phase field d and displacement $\mathbf{u}$ is hidden in the definition of the stress and history fields. We solve the equations in a staggered fashion, replacing $G_d(d,\mathbf{u})$ and $G_{\mathbf{u}}(\mathbf{u},d)$ by $G_d(d \mid \mathbf{u})$ and $G_{\mathbf{u}}(\mathbf{u} \mid d)$ respectively, and treating $\mathbf{u}$ as a parameter for the solution of d and vice versa. We iterate using the Newton–Raphson method, utilizing linearized weak forms (cf. [35]) with respect to their first variable, namely

$$\mathrm{Lin}[G_{\mathbf{u}}] = G_{\mathbf{u}} + D_{\mathbf{u}}[G_{\mathbf{u}}] \approx 0, \tag{A.3}$$

$$\mathrm{Lin}[G_d] = G_d + D_d[G_d] \approx 0, \tag{A.4}$$

with the linear increments of the weak forms given by

$$D_{\mathbf{u}}[G_{\mathbf{u}}] = \int_{\mathcal{B}} \mathrm{d}V \frac{\rho}{\Delta t_{n+1}^2}\delta\mathbf{u}\cdot\Delta\mathbf{u} + \int_{\mathcal{B}} \mathrm{d}V\, \delta\boldsymbol{\varepsilon} :\mathbb{C}:\Delta\boldsymbol{\varepsilon}, \tag{A.5}$$

$$D_d[G_d] = \int_{\mathcal{B}} \mathrm{d}V \left(\frac{G_c}{l} + 2\mathcal{H}\right)\delta d\,\Delta d + \int_{\mathcal{B}} \mathrm{d}V\, G_c l\, \nabla\delta d\cdot\nabla\Delta d, \tag{A.6}$$

in terms of the linear increments of the displacement and phase field, $\Delta\mathbf{u}$ and Δd respectively. The increment of the strain $\Delta\boldsymbol{\varepsilon}$ is defined in analogy to Eq. (7), replacing $\mathbf{u}$ by $\Delta\mathbf{u}$, and the fourth order stiffness tensor is given through $\mathbb{C} := \partial\boldsymbol{\sigma}/\partial\boldsymbol{\varepsilon}$. We follow a similar approach as in [36] to express it in terms of eigenvalues λ_i and eigenvectors $\boldsymbol{v}_i$ of the strain tensor

$$\mathbb{C} = \sum_{a,b=1}^{3} \frac{\partial s_b}{\partial \lambda_a}\, \boldsymbol{v}_b \otimes \boldsymbol{v}_b \otimes \boldsymbol{v}_a \otimes \boldsymbol{v}_a + \frac{1}{2} \sum_{\substack{a,b=1 \\ a\neq b}} \frac{s_b - s_a}{\lambda_b - \lambda_a} \left(\boldsymbol{v}_a \otimes \boldsymbol{v}_b \otimes \boldsymbol{v}_a \otimes \boldsymbol{v}_b + \boldsymbol{v}_a \otimes \boldsymbol{v}_b \otimes \boldsymbol{v}_b \otimes \boldsymbol{v}_a\right), \tag{A.7}$$

with s_i denoting an eigenvalue of the Cauchy stress tensor. Due to the isotropy of the free energy potential, the eigenvectors of the stress and strain tensor are co-linear and the eigenvalues may therefore be expressed as $s_i = \partial\psi/\partial\lambda_i$. Inserting (9), we write the terms in the above sum explicitly as

$$\frac{\partial s_b}{\partial \lambda_a} = g(d) \left[L \frac{\left\langle \sum_{j=1}^{3} \lambda_j \right\rangle_+}{\sum_{j=1}^{3} \lambda_j} + 2G\, \delta_{ab} \frac{\langle \lambda_b \rangle_+}{\lambda_b} \right] + \left[L \frac{\left\langle \sum_{j=1}^{3} \lambda_j \right\rangle_-}{\sum_{j=1}^{3} \lambda_j} + 2G\, \delta_{ab} \frac{\langle \lambda_b \rangle_-}{\lambda_b} \right], \tag{A.8}$$

$$\frac{s_b - s_a}{\lambda_b - \lambda_a} = g(d)\, 2G \frac{\langle \lambda_b \rangle_+ - \langle \lambda_a \rangle_+}{\lambda_b - \lambda_a} + 2G \frac{\langle \lambda_b \rangle_- - \langle \lambda_a \rangle_-}{\lambda_b - \lambda_a}. \tag{A.9}$$

In cases, where eigenvalues are zero or equal, the above expressions are understood in an asymptotic sense. Namely, it can be shown that as a denominator approaches zero, the corresponding enumerator tends to zero at the same rate. Each of the terms in Eqs. (A.7)–(A.9) is therefore well-defined and no singularities occur.

Eqs. (A.5) and (A.6) are discretized by substituting the fields, test functions and increments through linear combinations of shape functions N_j and nodal values $\mathbf{D}_j$ by

$$\mathbf{u} \approx \mathbf{u}^h = \sum_{j}^{\mathcal{N}} N_j(\mathbf{x}) \mathbf{D}_j^{\mathbf{u}} = \mathbf{N}\mathbf{D}^{\mathbf{u}}, \qquad \delta\mathbf{u} \approx \mathbf{N}\delta\mathbf{D}^{\mathbf{u}} \quad \text{and} \quad \Delta\mathbf{u} \approx \mathbf{N}\Delta\mathbf{D}^{\mathbf{u}}, \tag{A.10}$$

as well as

$$d \approx d^h = \sum_{j}^{\mathcal{N}} N_j(\mathbf{x}) D_j^{d} = \mathbf{N}\mathbf{D}^{d}, \qquad \delta d \approx \mathbf{N}\delta\mathbf{D}^{d} \quad \text{and} \quad \Delta d \approx \mathbf{N}\Delta\mathbf{D}^{d}. \tag{A.11}$$

They are then cast into matrix form as $\mathbf{R}_{\mathbf{u}} + \mathbf{K}_{\mathbf{uu}}\Delta\mathbf{D}^{\mathbf{u}} = \mathbf{0}$ and $\mathbf{R}_d + \mathbf{K}_{dd}\Delta\mathbf{D}^{d} = \mathbf{0}$ with the residual vectors and tangent matrices given by

$$\mathbf{R}_{\mathbf{u}} = \int_{\mathcal{B}} \mathrm{d}V \frac{\rho}{\Delta t_{n+1}^2} \mathbf{M}\left(\mathbf{D}^{\mathbf{u}} - \mathbf{D}_n^{\mathbf{u}}\right) - \int_{\mathcal{B}} \mathrm{d}V \frac{\rho}{\Delta t_{n+1}\Delta t_n} \mathbf{M}\left(\mathbf{D}_n^{\mathbf{u}} - \mathbf{D}_{n-1}^{\mathbf{u}}\right) + \int_{\mathcal{B}} \mathrm{d}V \left(\boldsymbol{\sigma}^h : \mathbf{S}\right)^T, \tag{A.12}$$

$$\mathbf{K}_{\mathbf{uu}} = \int_{\mathcal{B}} \mathrm{d}V \frac{\rho}{\Delta t_{n+1}^2} \mathbf{M} + \int_{\mathcal{B}} \mathrm{d}V \left(\boldsymbol{\sigma}^h : \mathbf{S}\right)^T : \mathbf{S}, \tag{A.13}$$

for the conservation of linear momentum and

$$\mathbf{R}_d = \int_{\mathcal{B}} \mathrm{d}V \left(\frac{g_c}{l} + 2\mathcal{H}^h\right) \mathbf{M}\,\mathbf{D}^d + \int_{\mathcal{B}} \mathrm{d}V g_c l\, \mathbf{B}^T\mathbf{B}\,\mathbf{D}^d, \tag{A.14}$$

$$\mathbf{K}_{dd} = \int_{\mathcal{B}} \mathrm{d}V \left(\frac{g_c}{l} + 2\mathcal{H}^h\right) \mathbf{M} + \int_{\mathcal{B}} \mathrm{d}V g_c l\, \mathbf{B}^T\mathbf{B}, \tag{A.15}$$

for the evolution of the phase field. Here, $\boldsymbol{\sigma}^h$ and $\mathcal{H}^h$ are the approximations to the Cauchy stress and history field, $\mathbf{M} = \mathbf{N}^T\mathbf{N}$ is the so called mass matrix at unit density, and $\mathbf{B}$ and $\mathbf{S}$ are ordered representations of tensors defined through $\nabla d \approx \nabla d^h = \nabla(\mathbf{N}\mathbf{D}^d) = (\nabla^T\mathbf{N})\mathbf{D}^d = \mathbf{B}\mathbf{D}^d$ and $\boldsymbol{\varepsilon} = \mathrm{sym}[\nabla\mathbf{u}] \approx \mathrm{sym}[\nabla\mathbf{u}^h] = \sum_j^{\mathcal{N}} \mathrm{sym}[N_j(\mathbf{x})\mathbf{D}_j^{\mathbf{u}}] = \sum_j^{\mathcal{N}} \mathbf{S}^j\mathbf{D}_j^{\mathbf{u}} = \mathbf{S}\mathbf{D}^{\mathbf{u}}$.

A.2. Mesh adaption scheme

The refinement and coarsening conditions described in Section 3 are implemented in a mesh adaption scheme, which runs over all elements and flags them correspondingly. For each element, the algorithm performs the following steps:

1. Loop over all quadrature points $\mathbf{q}_i \in \mathcal{Q}$ and find the maximum energy and gradient norm $\max_{\mathbf{q}_i \in \mathcal{Q}} \psi^+_{\text{mech}}$ and $\max_{\mathbf{q}_i \in \mathcal{Q}} |\nabla d|$.
2. Compute the element size h as the maximum element diameter divided by the root of the number of dimensions.
3. Compute the threshold energy for refinement and coarsening
   (a) If $h \leq h_{\max}$, $\psi^{\text{refine}}_{\text{thresh}} = \tilde{\psi}_{\text{thresh}}(h)$ and $\psi^{\text{coarsen}}_{\text{thresh}} = \tilde{\psi}_{\text{thresh}}(h/2^{\Delta n})$.
   (b) Else, $\psi^{\text{refine}}_{\text{thresh}} = \tilde{\psi}_{\text{thresh}}(h_{\max})$ and $\psi^{\text{coarsen}}_{\text{thresh}} = \tilde{\psi}_{\text{thresh}}(h_{\max}/2^{\Delta n})$.
4. For every element, set refinement and coarsening flags according to the following rules:
   (a) If $\max_{\mathbf{q}_i \in \mathcal{Q}} \psi^+_{\text{mech}} > \psi^{\text{refine}}_{\text{thresh}}$ and $h > h_{\min}$, flag for refinement.
   (b) Else if $\max_{\mathbf{q}_i \in \mathcal{Q}} |\nabla d| > k_1/h$, flag for refinement.
   (c) Else if $\max_{\mathbf{q}_i \in \mathcal{Q}} \psi^+_{\text{mech}} < \psi^{\text{coarsen}}_{\text{thresh}}$ and $\max_{\mathbf{q}_i \in \mathcal{Q}} |\nabla d| < k_2/h$, flag for coarsening.
   (d) Else, clear any refinement or coarsening flag.

After having gone through all elements, the algorithm may flag further elements to generate a smoother mesh and to avoid unfavorable element groupings, e.g. isolated refined elements, that may lead to degradation of the numerical approximation. Elements flagged for refinement are then divided into four (eight) new 2D quadrilateral (3D hexahedral) elements. Hanging nodes, i.e. nodes that belong only to one of their adjacent elements, are treated by appropriate constraints. The algorithms for these steps are provided by deal.II.

References

[1] T.L. Anderson, Fracture Mechanics, CRC Press, 1995.
[2] T. Rabczuk, Computational methods for fracture in brittle and quasi-brittle solids: State-of-the-art review and future perspectives, ISRN Appl. Mech. 849231 (2013) 1–38.
[3] C. Miehe, F. Welschinger, M. Hofacker, Thermodynamically-consistent phase field models of fracture: Variational and multi-field FE implementations, Internat. J. Numer. Methods Engrg. 83 (10) (2010) 1273–1311.
[4] M.J. Borden, T.J.R. Hughes, C.M. Landis, C.V. Verhoosel, A higher-order phase-field model for brittle fracture: Formulation and analysis within the isogeometric analysis framework, Comput Methods Appl. Mech. Engrg. 273 (2014) 100–118.
[5] R. de Borst, J.J.C. Remmers, A. Needleman, M.-A. Abellan, Discrete vs smeared crack models for concrete fracture: bridging the gap, Int. J. Numer. Anal. Methods Geomech. 28 (7–8) (2004) 583–607.
[6] H. Amor, J.-J. Marigo, C. Maurini, Regularized formulation of the variational brittle fracture with unliateral contact: Numerical experiments, J. Mech. Phys. Solids 57 (2009) 1209–1229.
[7] A.R. Ingraffea, V. Saouma, Numerical Modeling of Discrete Crack Propagation in Reinforced Plain Concrete, in: Fracture mechanics of concrete: Structural application and numerical calculation, Vol. 4, 1985, pp. 171–225.
[8] N. Moës, J. Dolbow, T. Belytschko, A finite element method for crack growth without remeshing, Internat. J. Numer. Methods Engrg. 46 (1999) 131–150.
[9] M. Ortiz, A. Pandolfi, Finite-Deformation irreversible cohesive elements for three-dimensional crack-propagation analysis, Internat. J. Numer. Methods Engrg. 44 (1999) 1267–1282.
[10] X.-P. Xu, A. Needleman, Numerical simulations of fast crack growth in brittle solids, J. Mech. Phys. Solids 42 (9) (1994) 1397–1434.
[11] M. Borden, C. Verhoosel, M. Scott, T. Hughes, C. Landis, A phase-field description of dynamic brittle fracture, Comput. Methods Appl. Mech. Engrg. 217–220 (2012) 77–95.
[12] M. Hofacker, C. Miehe, Continuum phase field modeling of dynamic fracture: variational principles and staggered FE implementation, Int. J. Fract. 178 (2012) 113–129.
[13] M. Hofacker, C. Miehe, A phase field model of dynamic fracture: Robust field updates for the analysis of complex crack patterns, Internat. J. Numer. Methods Engng 93 (2013) 276–301.
[14] C. Kuhn, R. Müller, Phase field simulation of thermomechanical fracture, Proc. Appl. Math. Mech. 9 (2009) 191–192.
[15] C. Miehe, F. Welschinger, M. Hofacker, A phase field model of electromechanical fracture, J. Mech. Phys. Solids 58 (2010) 1716–1740.
[16] C. Kuhn, R. Müller, A continuum phase field model for fracture, Eng. Fract. Mech. 77 (2010) 3625–3634.
[17] A.A. Griffith, The phenomena of rupture and flow in solids, Philos. Trans., Ser. A 221 (1920) 163–198.
[18] G.R. Irwin, Fracture Dynamics, in: Fracturing of Metals, American Society for Metals, 1948, p. 152.
[19] G. Francfort, J.-J. Marigo, Revisiting brittle fracture as an energy minimization problem, J. Mech. Phys. Solids 46 (8) (1998) 1319–1342.
[20] B. Bourdin, G.A. Francfort, J.-J. Marigo, Numerical experiments in revisited brittle fracture, J. Mech. Phys. Solids 48 (2000) 797–826.
[21] L. Ambrosio, V.M. Tortorelli, Approximation of functionals depending on jumps by elliptic functionals via γ-convergence, Comm. Pure Appl. Math. 43 (1990) 999–1036.

[22] D. Mumford, J. Shah, Optimal approximations by piecewise smooth functions and associated variational problems, Comm. Pure Appl. Math. 42 (1989) 577–685.
[23] B. Bourdin, G.A. Francfort, J.-J. Marigo, The variational approach to fracture, J. Elasticity 91 (1–3) (2008) 5–148.
[24] C. Miehe, M. Hofacker, F. Welschinger, A phase field model for rate-independent crack propagation: Robust algorithmic implementation based on operator splits, Comput. Methods Appl. Mech. Engrg. 199 (2010) 2765–2778.
[25] G.D. Piero, G. Lancioni, R. March, A variational model for fracture mechanics: Numerical experiments, J. Mech. Phys. Solids 55 (2007) 2513–2537.
[26] G. Lancioni, G. Royer-Carfagni, The variational approach to fracture mechanics. A practical application to the French Panthéon in Paris, J. Elasticity 1–2 (95) (2009) 1–30.
[27] W. Bangerth, R. Hartmann, G. Kanschat, deal.II — a general purpose object oriented finite element library, ACM Trans. Math. Software 33 (4) (2007) 24.
[28] W. Bangerth, C. Burstedde, T. Heister, M. Kronbichler, Algorithms and data structures for massively parallel generic adaptive finite element codes, ACM Trans. Math. Software 38 (14) (2011) 1–28.
[29] M.A. Heroux, R.A. Bartlett, V.E. Howle, R.J. Hoekstra, J.J. Hu, T.G. Kolda, R.B. Lehoucq, K.R. Long, R.P. Pawlowski, E.T. Phipps, A.G. Salinger, H.K. Thornquist, R.S. Tuminaro, J.M. Willenbring, A. Williams, K.S. Stanley, An overview of the Trilinos project, ACM Trans. Math. Software 31 (3) (2005) 397–423.
[30] S. Balay, W.D. Gropp, L.C. McInnes, B.F. Smith, Modern Software Tools in Scientific Computing — Efficient Management of Parallelism in Object Oriented Numerical Software Libraries, Birkhäuser Press, 1997.
[31] J. Nocedal, S. Wright, Numerical Optimization, in: Springer Series in Operations Research and Financial Engineering, Springer Verlag, 2006.
[32] H. Tada, P.C. Paris, G.R. Irwin, The Stress Analysis of Cracks Handbook, Professional Engineering Publishing, 2000.
[33] J. Lemaitre, A Course on Damage Theory, Springer Verlag, 1996.
[34] B. Bourdin, Numerical implementation of the variational formulation for quasi-static brittle fracture, Interfaces Free Bound. 9 (2007) 411–430.
[35] G.A. Holzapfel, Nonlinear Solid Mechanics: A Continuum Approach for Engineering, Wiley, 2000.
[36] J. Bonet, R.D. Wood, Nonlinear Continuum Mechanics For Finite Element Analysis, Cambridge University Press, 1997.